ACS APPLIED MATERIALS & INTERFACES

Research Article

www.acsami.org

# Excitation Wavelength Independence: Toward Low-Threshold Amplified Spontaneous Emission from Carbon Nanodots

Yongqiang Zhang,[†,‡] Yongsheng Hu,*[,†] Jie Lin,[†] Yi Fan,*[,†] Yantao Li,[†] Ying Lv,[†] and Xingyuan Liu*[,†]

[†]State Key Laboratory of Luminescence and Applications, Changchun Institute of Optics, Fine Mechanics, and Physics, Chinese Academy of Sciences, Changchun 130033, China

[‡]University of Chinese Academy of Sciences, Beijing 100049, China

*Supporting Information*

**ABSTRACT:** Carbon nanodots (CDs) are known to be a superior type of lasing material due to their low cost, low toxicity, high photostability, and photobleaching resistance. Significant attention has been paid to synthesizing CDs with high fluorescence quantum yields (FLQYs) to achieve higher optical gains. In this report, we reveal that excitation wavelength-independent ($\lambda_{ex}$-independent) photoluminescence (PL) characteristics, rather than high FLQYs, should be given priority to realize CD-based light amplification. CDs with excitation wavelength-dependent ($\lambda_{ex}$-dependent) PL characteristics and FLQYs as high as 99% and 96% were found not to exhibit amplified spontaneous emission (ASE), while those with $\lambda_{ex}$-independent PL characteristics and FLQYs of only 38% and 82% realized ASE with low thresholds. The difficulty of achieving ASE using CDs with $\lambda_{ex}$-dependent PL characteristics is likely attributable to their high contents of C−O−H or C−O−C groups. These groups can induce numerous localized electronic states within the n−$\pi$* gap, which could decentralize the excited electrons, thus increasing the difficulty of population inversion. In addition, the radiative transition rates and stimulated emission cross sections of CDs with $\lambda_{ex}$-independent PL characteristics were found to be significantly higher than those of CDs with $\lambda_{ex}$-dependent PL characteristics. ASE in a planar waveguide structure, which is a practical structure for solid-state lasing devices, was also demonstrated for the first time using CDs with $\lambda_{ex}$-independent PL characteristics. These results provide simple and effective guidelines for synthesizing and selecting CDs for low-threshold lasing devices.

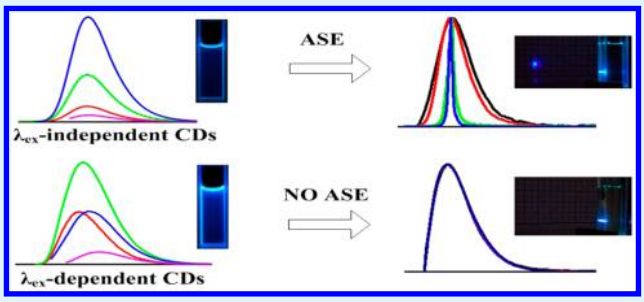


**KEYWORDS:** *carbon nanodots (CDs), excitation-independent, amplified spontaneous emission (ASE), lasing, planar waveguide*

## INTRODUCTION

As a new type of organic luminescent quantum dots (QDs), carbon nanodots (CDs) have attracted great interest due to their advantages of low cost, low toxicity, chemical inertness, and photobleaching resistance.[1−5] With the achievement of ultrahigh (∼100%) fluorescence quantum yields (FLQYs) in the past few years,[6,7] CDs have great potential for use in applications such as bioimaging,[8−11] fluorescence encryption,[12,13] white light-emitting diodes,[14,15] and photocatalysts.[16] CDs have also been demonstrated to be promising as lasing materials whose emission wavelengths ($\lambda_{em}$) can be tuned in the entire visible wavelength range,[17−19] which will inevitably expand their applications.

Generally, it is believed that a high FLQY and low optical loss are the two factors determining the lasing capabilities of CDs.[20−22] Therefore, significant attention has been paid to synthesizing CDs with high FLQYs and building cavities with high quality factors (Q) to lower the lasing threshold. The first CD-based lasing was reported by Yu and co-workers, who used a high-Q cylindrical fiber microcavity coated with polyethylene-glycol-modified CDs.[20] Qu et al. observed green lasing from a CD ethanol aqueous solution in a long linear Fabry−Perot cavity and claimed that the high FLQY and low self-absorption were responsible for the lasing.[22] Despite these pioneering works, the type of CD that is more suitable for lasing or amplified spontaneous emission (ASE) remains unclear, especially under the premise that many CDs with high FLQYs did not exhibit ASE in our experiments. Moreover, CD-based solid-state lasing is still in high demand.

Unlike conventional fluorophores such as organic dyes and inorganic QDs whose photoluminescence (PL) characteristics follow Kasha's rule[23] that an excited electron will always return to the lowest excited state through nonradiative relaxation and will then undergo radiative recombination to return to the ground state, resulting in $\lambda_{em}$ being independent of the excitation wavelength ($\lambda_{ex}$-independent), the PL characteristics of CDs can be either $\lambda_{ex}$-independent or $\lambda_{ex}$-dependent. In most cases, these characteristics are $\lambda_{ex}$-dependent since numerous energy levels originating from the effects of the multiple O-containing functional groups will appear in the n−$\pi$* gap.[24]

**Received:** July 7, 2016
**Accepted:** September 12, 2016
**Published:** September 12, 2016





DOI: 10.1021/acsami.6b08315
ACS Appl. Mater. Interfaces 2016, 8, 25454−25460

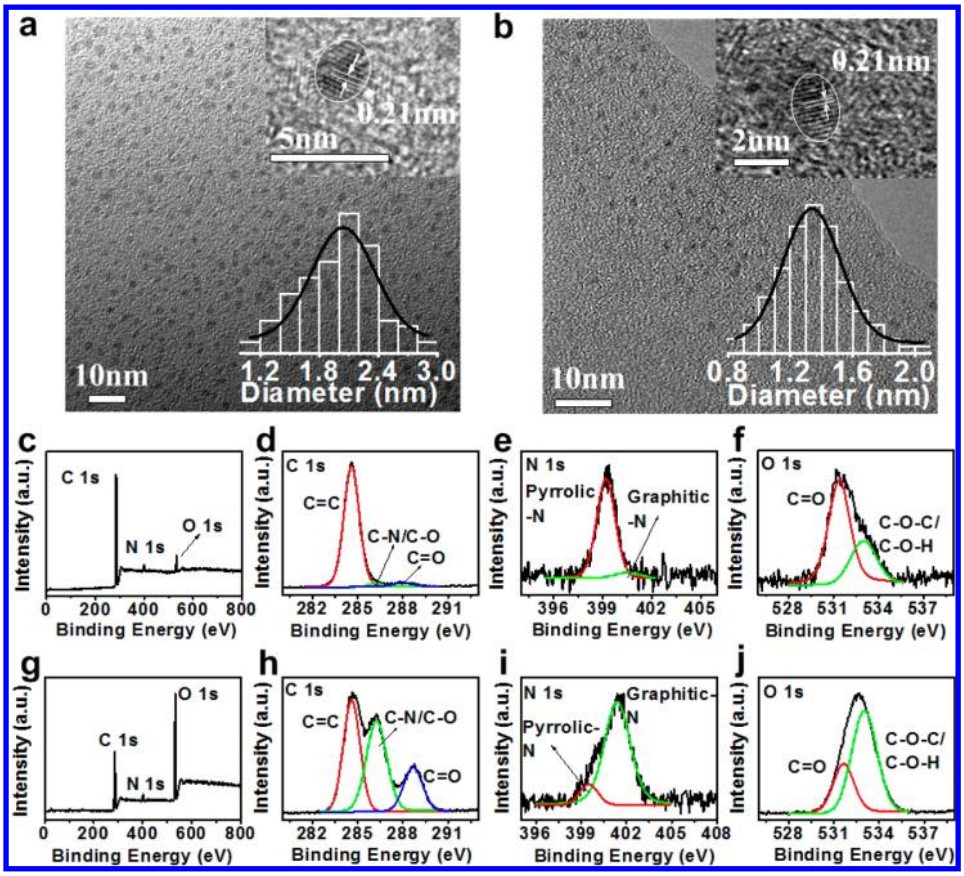


**Figure 1.** Transmission electron microscopy (TEM) images of (a) CD1 and (b) CD2 (upper insets are high-resolution TEM (HRTEM) images, lower insets are size distribution histogram). (c) X-ray photoelectron spectroscopy (XPS) full scan, (d) C 1s, (e) N 1s, and (f) O 1s of CD1, and (g) XPS full scan, (h) C 1s, (i) N 1s, and (j) O 1s of CD2.

Generally, CDs with $\lambda_{ex}$-independent PL characteristics can be synthesized by controlling the synthetic method,[25,26] reactant ratio,[3] reaction temperature,[6] heating time,[27] and purification.[28]

In this study, two groups of CDs with $\lambda_{ex}$-independent and $\lambda_{ex}$-dependent PL characteristics and different FLQYs were synthesized and investigated. It was determined that $\lambda_{ex}$-independent PL characteristics, rather than high FLQYs, should be given priority to realize CD-based ASE. ASE was not observed for the CDs with $\lambda_{ex}$-dependent PL characteristics even though they had high FLQYs of 99% and 96%, whereas ASE with a relatively low threshold was observed for the CDs with $\lambda_{ex}$-independent PL characteristics, whose FLQYs were only 38% and 82%. The C−O−H/C−O−C groups were determined to play an important role in resulting $\lambda_{ex}$-dependent PL characteristics since they can induce numerous localized electronic states within the n−$\pi$* gap, which could decentralize the excited electrons, thus increasing the difficulty of population inversion. It was also found that the radiative transition rates ($K_R$) and the stimulated emission cross section (SECs) of the CDs with $\lambda_{ex}$-independent PL characteristics were significantly higher than those of the CDs with $\lambda_{ex}$-dependent PL characteristics. Moreover, CD-based ASE was achieved for the first time in a planar waveguide structure, which is a practical structure for future solid-state laser device applications.

## ■ MATERIALS AND METHODS

**Materials.** Citric acid monohydrate (CA), tris(hydroxylmethyl)-aminomethane (Tris), L-cysteine, and ethanolamine (EA) were purchased from Sinopharm Chemical Reagent Co. Ltd. Sodium hydroxide, ethanol, sulfuric acid, and urea were purchased from Beijing Chemical Works. All of the chemicals are commercially available and of analysis-grade purity without further purification. The ultrapure water used in all of the experiments was from a Millipore system.

**Synthesis of CD1.** First, 1.5 g of sodium hydroxide and 0.38 g of urea were added to an ethanol aqueous solution (100 mL of anhydrous ethanol and 30 mL of ultrapure water), which was ultrasonically treated so that it would become transparent. Two C rods were immerged in the solution to form a dual-electrode system (Figure S1 of the Supporting Information). The initial potential was set at 5 V, and the current was kept in the range of 30−40 mA. The electrochemical process lasted 24 h, during which the color of the solution changed from transparent to deep brown. Then 100 mL of $H_2SO_4$ solution (0.35 mol/L) was added to the solution, followed by stewing for 12 h. Finally, the solution was freeze-dried to powder.

**Synthesis of CD2.** First, 3.5 g of CA and 2 g of Tris were added to 20 mL of ultrapure water, and the solution was ultrasonically treated so that it would become transparent. The solution was transferred to a domestic microwave oven and heated at 350 W for 5 min (the heating curve is shown in Figure S2). The first three heating periods were performed to remove the water quickly, and regular pauses were taken between heating periods to avoid sudden boiling. Heating was subsequently performed for a short period to prevent uneven carbonization from being caused by rapid heating and then for additional periods to achieve further carbonization of the unreacted polymeric structures. Stirring and shaking were necessary during the intervals between the heating periods to ensure the homogeneity of the reactions. The products were collected by adding an appropriate amount of ultrapure water and centrifuging at 5000 rpm (1660*g*, where *g* is the acceleration of gravity) for 5 min to remove the aggregate precipitate. Finally, the solution was freeze-dried to powder.


DOI: 10.1021/acsami.6b08315
ACS Appl. Mater. Interfaces 2016, 8, 25454−25460

Table 1. Amounts of Different Types of Chemical Bonds in the CDs Used in This Work

| | C 1s | | | N 1s | | O 1s | |
|---|---|---|---|---|---|---|---|
| sample | C=C | C−N/C−O | C=O | pyrrolic-N | graphitic-N | C=O | C−OH/C−O−C |
| CD1 | 0.93 | 0.02 | 0.05 | 0.032 | 0.003 | 0.038 | 0.027 |
| CD2 | 0.42 | 0.42 | 0.16 | 0.007 | 0.055 | 0.190 | 0.432 |
| CD3 | 0.45 | 0.29[a] | 0.26 | 0.056 | 0.014 | 0.194 | 0.118 |
| CD4 | 0.46 | 0.35 | 0.19 | 0.034 | 0.050 | 0.204 | 0.306 |

[a]C−N/C−O/C−S.

**Synthesis of CD3.** After 3 g of CA and 2 g of L-cysteine were added to 20 mL of ultrapure water, the same process that was used to synthesize CD2 was followed.

**Synthesis of CD4.** After 3.5 g of CA and 1 mL of EA were added to 20 mL of ultrapure water, the same process that was used to synthesize CD2 was followed.

**Preparation of the CDs Solution.** The as-prepared CDs were redissolved in ethanol aqueous solution (the volume ratio for ethanol and water is 3:1) with the concentration of 5 mg/mL.

**Preparation of CD1/Polyimide (PI) Film.** The as-prepared CD1 solution was mixed with PI (in a volume ratio of 3:1), stirred for 30 min, and then treated ultrasonically at 60 °C for 1 h to form a homogeneous CD1/PI solution. A CD1/PI film was prepared by spin-coating at 2000 rpm (265.6*g*) for 40 s and was annealed at 80 °C for 1 h.

**Characterizations.** High-resolution transmission electron microscope (HRTEM) images and fast Fourier transform (FFT) spot diagrams were recorded by FEI-TECNAI G2 TEM operating at 200 kV. X-ray photoelectron spectra (XPS) were obtained by Thermo Scientific ESCALAB 250 Multitechnique Surface Analysis. Fourier Transform Infrared (FT-IR) spectra were recorded using KBr tablets with a Bio-Rad Excalibur FTS3000 spectrometer (4000−1000 $cm^{-1}$). UV−vis absorption spectra were conducted on Shimadzu UV-3101 PC spectrophotometer. Fluorescence emission spectra were recorded by Hitachi fluorescence spectrophotometer F-7000. Absolute fluorescent quantum yield measurements were performed with a calibrated integrating sphere on FLS920 spectrometer (Figure S3−S6). The FLQYs determined by the slope method were obtained by using the reference of quinine sulfate (Figure S7 and Table S1). The net gain measurement by Variable Stripe Length (VSL) technique and optical pumping investigations were performed using a Nd:YAG laser ($\lambda$ = 355 nm, pulse width 10 ns at 1 Hz repetition rate). The pumping laser beam was focused into a 0.4 × 10 $mm^2$ rectangular stripe by a cylindrical lens and the pumping fluence was tuned by a set of calibrated neutral density filters. The ASE emission spectra were obtained using an Ocean Optics Maya2000 Pro Fiber Optic Spectrometer. The pumping fluence was recorded using a Newport 2936C laser power meter. All measurements were performed at room temperature under ambient conditions.

## RESULTS AND DISCUSSION

CD1, which had $\lambda_{ex}$-independent PL characteristics and an FLQY of 38%, and CD2, which had $\lambda_{ex}$-dependent PL characteristics and an FLQY of 99%, were compared first. (a) and (b) of Figure 1 show TEM images of CD1 and CD2, respectively. Both CD1 and CD2 have quasi-spherical shapes and are uniformly distributed without aggregation. The HRTEM images (upper insets in Figure 1a,b) of CD1 and CD2 reveal a lattice spacing of 2.1 Å, which corresponds to the in-plane lattice spacing of graphite (100 facet).[3] The lower insets in Figure 1a,b present the corresponding size distribution histograms. The sizes vary from 1.0 to 3.0 nm with a mean value of around 2.04 nm and from 0.8 to 2.1 nm with a mean value of around 1.34 nm for CD1 and CD2, respectively. Both size distributions are approximately Gaussian, which is in agreement with the literature.[29] XPS was then performed to determine the compositions of the CDs. The full XPS spectra of CD1 and CD2 (Figures 1c,g, respectively) exhibit peaks at 285.0, 400.0, and 533 eV, which correspond to C 1s, N 1s, and O 1s, respectively.[30] The high-resolution C 1s scans (Figure 1d,h) show four different chemical bonds, corresponding to $sp^2$ C of C=C in C at 284.6 eV, $sp^3$ C in C−N/C−O at 286.5 eV, and $sp^3$ C C=O around 288 eV, respectively. The high-resolution N 1s scans (Figure 1e,i) reveal two different types of N doping: pyrrolic N at 398.2−399.5 eV and graphitic N at 400.5−401.5 eV.[31,32] The O 1s spectra (Figure 1f,j) exhibit peaks at 531.8 and 533 eV, corresponding to C=O and C−OH/C−O−C groups, respectively.[33,34] We also extracted the amounts of the different types of chemical bonds in the different CDs (see Table 1). It is notable that the C−N/C−O bond and graphitic-N contents of CD2 are about 20 times greater than those of CD1. The N mainly exists in the form of graphitic N, while the C−O bonds mainly exist in the form of C−O−C groups and unreacted hydroxyl moieties in CD2. Since it is common to promote the FLQYs of CDs by introducing graphitic N and hydroxyl moieties,[6,35,36] we expect that the high contents of C−N/C−O bonds and graphitic N are the main reasons for the ultrahigh FLQY of CD2. The chemical bond compositions of CD1 and CD2 were also characterized by obtaining FT-IR spectra (Figure S8), which apparently show the stretching vibrations of C−O at 1200 and 1050 $cm^{-1}$ and the bending vibrations of N−H and O−H at 1585 and 1384 $cm^{-1}$.[37,38] Again, the C−O intensity of CD2 is much greater than that of CD1.

Parts (a) and (b) of Figure 2 present contour plots of the PL spectra of CD1 and CD2 solutions, respectively. A blue $\lambda_{ex}$-independent PL emission band with a peak wavelength of 450 nm is observed for CD1 as the excitation wavelength varies from 300 to 420 nm. In contrast, the peak $\lambda_{em}$ of CD2 changes from 400 to 430 nm as $\lambda_{ex}$ increases from 300 to 380 nm. The photoluminescence excitation (PLE) spectra of these CDs were provided in Figure S9. It is well-known that there are $\pi-\pi^*$ and $n-\pi^*$ transitions in CDs; however, the $n-\pi^*$ transition is more likely to predominate due to the existence of C=O bonds.[39] According to the first-principle calculations by Yan et al., the C−O−C and C−O−H groups of $sp^2$-hybridized C can induce significant local distortions and create various energy levels.[40] Therefore, as the numbers of C−O−H and C−O−C groups in the CDs increase, more hydroxy (or epoxide)-related localized electronic states are expected to form below the $\pi^*$ state, creating numerous new energy levels within the $n-\pi^*$ gap (Figure 2c).[41] Since CD1 contains few C−O−H/C−O−C groups, its energy-level diagram can be depicted as shown in the left part of Figure 2c. The electrons from the ground state (n) are excited to a high excited state ($\pi^*$), undergo thermal relaxation to the lowest excited state ($\pi^*$) and further to the C−O−H/C−O−C-related localized electronic states, and finally transition back to the ground state and emit photons. In this case, it is reasonable that $\lambda_{em}$ does not depend on the


DOI: 10.1021/acsami.6b08315
ACS Appl. Mater. Interfaces 2016, 8, 25454−25460

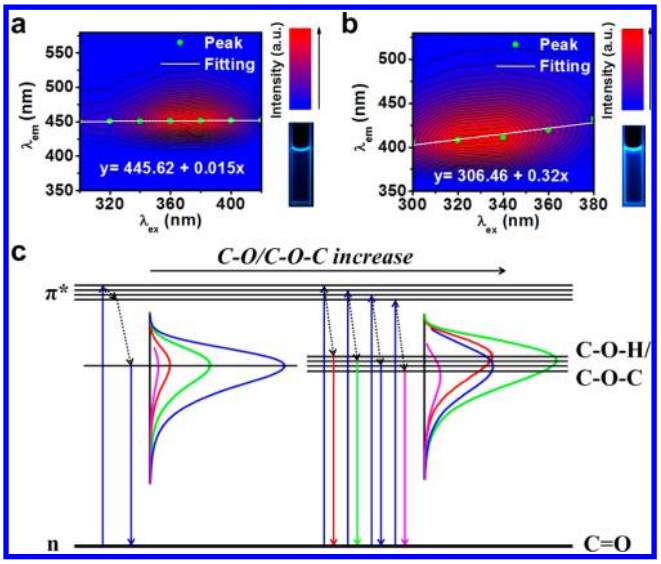


**Figure 2.** Contour plots of PL spectra of (a) CD1 and (b) CD2 solutions. The insets are fluorescence images of CD1 and CD2 excited using a 365 nm UV lamp. (c) Energy-level diagrams of CDs with $\lambda_{ex}$-independent and $\lambda_{ex}$-dependent PL characteristics.

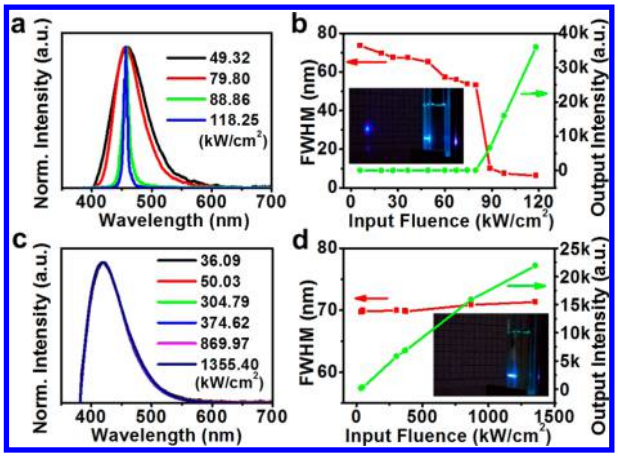


**Figure 3.** ASE characteristics of CDs solutions. Normalized emission spectra of (a) CD1 and (c) CD2 under different pumping fluences. Dependence of the output peak intensity and full-width at half-maximum (fwhm) on the pumping fluence for (b) CD1 and (d) CD2 solutions. The insets in (b) and (d) are the operating devices pumped at 355 nm for CD1 and CD2 solutions, respectively.

excitation energy since all of the excited electrons, independent of their initial energies, will relax to the lowest C−O−H/C−O−C-related localized electronic states before fluorescence proceeds, which is quite similar to the behavior of conventional fluorophores, which follows Kasha's rule.

The energy-level diagram of CD2 could be quite different because of its high content of C−O−H/C−O−C groups, as shown in the right part of Figure 2c, where numerous C−O−H/C−O−C-related localized electronic states appear below the $\pi^*$ state. The electrons from the ground state (n) are excited to the different vibrational energy levels of $\pi^*$ by different $\lambda_{ex}$, then relax to the corresponding energy levels of C−O−H/C−O−C-related localized electronic states, and finally transition back to the ground state, resulting in $\lambda_{ex}$-dependent PL characteristics.[24] The above physical process can be interpreted further based on the relationship between $\lambda_{em}$ and $\lambda_{ex}$ for CD2, which can be fitted by the linear equation $\lambda_{em} = 306.46 + 0.32\lambda_{ex}$. The existence of a linear relationship suggests that the slope, $\Delta\lambda_{em}/\Delta\lambda_{ex}$, where $\Delta\lambda_{em}$ and $\Delta\lambda_{ex}$ are the changes of the peak $\lambda_{em}$ and $\lambda_{ex}$, respectively, remains constant. Although there is a linear relationship between $\lambda_{em}$ and $\lambda_{ex}$ for CD1, the slope (0.015) is much smaller than that of CD2, which indicates that the C−O−H/C−O−C-related localized electronic states in CD1 are relatively centralized.

We next investigated the ASE characteristics of CD1 and CD2 solutions. The CDs solutions were transversely pumped using the experimental setup depicted in Figure S10. Figure 3a shows the edge emission spectra of CD1 corresponding to different pumping fluences. The fwhm obviously decreases with increasing pumping fluence. For a pumping fluence of about 120 kW/cm$^2$, the spectrum exhibits a peak at 458 nm with a fwhm of 4 nm. Figure 3b depicts the relationships between the pumping fluence and the peak output intensity as well as the fwhm and shows a clear ASE threshold of about 80 kW/cm$^2$, which is less than half of that reported by Qu et al.[22] A clear blue ASE spot is evident orthogonal to the pumping beam direction above the threshold (inset in Figure 3b). Figure 3c shows the normalized emission spectra of CD2 corresponding to different pumping fluences. Unlike the PL spectra of CD1, those of CD2 remain unchanged even when the pumping fluence reaches as high as 1350 kW/cm$^2$ (Figure 3c,d), which exceeds the damage threshold for ordinary CDs, and no ASE spot is observable (inset in Figure 3d). We also estimated the net gain of CD1 and CD2 solutions using the VSL technique.[42,43] As is shown in Figure S11, CD1 shows the net gain coefficients of 19.7 ± 0.4 and 24.7 ± 0.5 cm$^{-1}$ under the input influence of 90 and 115 kW/cm$^2$, respectively, whereas CD2 shows a negative net gain coefficient of −5.4 ± 0.2 cm$^{-1}$ under the pumping fluence as high as 1246 kW/cm$^2$. These results suggest that it is much more difficult for CDs with $\lambda_{ex}$-dependent PL characteristics to realize ASE than it is for CDs with $\lambda_{ex}$-independent PL characteristics, even if the FLQY is higher. We propose that the numerous C−O−H/C−O−C-related localized electronic states play an important role since these energy levels can decentralize the excited electrons, making it difficult to achieve population inversion. Besides, the higher content of C−O−H/C−O−C groups for CD2 may cause increased defects which would also quench the ASE.[44,45] It is worth emphasizing that this rule is universal for CDs; for example, it is applicable to CD3, which had $\lambda_{ex}$-independent PL characteristics and an FLQY of 82%, and to CD4, which had $\lambda_{ex}$-dependent PL characteristics and an FLQY of 96%, whose TEM and HRTEM images are shown in Figure S12. The ASE threshold of CD3 was determined to be about 350 kW/cm$^2$ (Figure S13), whereas no spectral narrowing was observed for CD4 even when a pumping fluence of 1385 kW/cm$^2$ was used. The FT-IR and XPS analysis results for CD3 and CD4 are presented in Figures S14 and S15. The amounts of C−N/C−O, graphitic N, and C−O−H/C−O−C groups in CD4 are significantly higher than those in CD3 (also see Table 1); these amounts are also strongly correlated with the FLQYs and PL properties of CD3 and CD4. CD3 shows quasi-$\lambda_{ex}$-independent PL characteristics with a $\Delta\lambda_{em}/\Delta\lambda_{ex}$ value of only 0.03 (Figure S16a and Table 2), which is slightly higher than that of CD1 (0.015), and obviously lower than that of CD4 (0.23) (Figure S16b and Table 2). In addition, it is worth mentioning that Qu et al.[22] reported that CDs with near-$\lambda_{ex}$-independent PL characteristics realized ASE, while those with $\lambda_{ex}$-dependent PL characteristics did not; these findings agree well with our results.


DOI: 10.1021/acsami.6b08315
ACS Appl. Mater. Interfaces 2016, 8, 25454−25460

**Table 2. Basic Chemical, Physical, and Optical Characteristics of the CDs Used in This Work**

| sample | PL characteristics | C−O−H/C−O−C | $\Delta\lambda_{em}/\Delta\lambda_{ex}$ | threshold (kW/cm$^2$) | $K_R$ ($\times 10^7$ s$^{-1}$) | SEC ($\times 10^{-17}$cm$^2$) | ESEC ($\times 10^{-17}$cm$^2$) |
|---|---|---|---|---|---|---|---|
| CD1 | independent | 0.027 | 0.015 | 80 | 9.5 | 4.65 | 3.22 |
| CD2 | dependent | 0.432 | 0.32 | N/A | 6.7 | 1.99 | 0.71 |
| CD3 | independent | 0.118 | 0.030 | 350 | 7.0 | 2.76 | 1.93 |
| CD4 | dependent | 0.306 | 0.23 | N/A | 6.5 | 2.08 | 0.68 |

For common organic luminescent materials, it has been shown that the ASE threshold is not directly correlated with the FLQY but that it is strongly correlated with $K_R$ and the SEC, since $K_R$ is related to Einstein's coefficient $B$ by $B \propto \frac{c^3}{8\pi h\nu_0^3}K_R$, where $h$ is Planck's constant, $\nu_0$ is the frequency of light, and $c$ is the speed of light; the ASE threshold is inversely proportional to $B$.[46,47] To investigate whether the relationship is applicable to CDs, the corresponding values of $K_R$ and the SEC ($\sigma_{em}$) were calculated by using[40] $K_R = \varphi/\tau$ and $\sigma_{em}(\lambda) = \frac{\lambda^4}{8\pi n^2 c_0 \tau}g(\lambda)$, where $\varphi$ is the FLQY, $\tau$ is the average fluorescence lifetime (in nanoseconds), which was measured (Figure S17) to be 4.00, 14.73, 11.70, and 14.78 ns for CD1, CD2, CD3, and CD4, respectively, $\lambda$ is the emission wavelength (in nanometers), $n$ is the refractive index (which was equal to 1.36 in this experiment), $c_0$ is the speed of light ($3 \times 10^8$ m/s), and $g(\lambda)$ is a linear function of spontaneous emission with $\int_0^\infty g(\lambda)\, d\lambda = \varphi$.[46] $K_R$ was determined to be $9.5 \times 10^7$, $6.7 \times 10^7$, $7.0 \times 10^7$, and $6.5 \times 10^7$ s$^{-1}$, while the maximum SECs were found to be $4.65 \times 10^{-17}$, $1.99 \times 10^{-17}$, $2.76 \times 10^{-17}$, and $2.08 \times 10^{-17}$ cm$^2$ for CD1, CD2, CD3, and CD4, respectively (Figure S18, Table 2). These values are similar to those of common organic luminescent materials.[48] $K_R$ and the SECs of CD1 and CD3 are higher than those of CD2 and CD4, which indicates a strong correlation with the ASE threshold.

The steady-state absorption cross section (ACs: $\sigma_a$) of the four kinds of CDs were shown in Figure S18, calculated by $\sigma_a(\lambda) = \frac{2.3A}{clN_A} \times 10^3$ (in square centimeters), where $A$ is the unitless absorbance, $c$ is the concentration (in moles per liter), $l$ is the optical path length (in centimeters), and $N_A$ is Avogadro's constant ($6.02 \times 10^{23}$).[49] To facilitate comparison, the effective stimulated emission cross section (ESEC, defined as the difference between the SECs and ACs) were also calculated and are presented in Figure S19. The maximum ESECs for CD1 and CD3 are $3.22 \times 10^{-17}$ and $1.93 \times 10^{-17}$ cm$^2$, respectively, which are higher than that of CD2 ($0.71 \times 10^{-17}$ cm$^2$) and CD4 ($0.68 \times 10^{-17}$ cm$^2$), indicating that it is more difficult to realize ASE for CD2 and CD4, which agrees well with the experiments.

Finally, we demonstrated that CD1 could also exhibit ASE when it was in a solid state. The ASE experimental setup is depicted in Figure S20, where a planar waveguide structure composed of CD1/PI film was used. The UV/vis and PL emission spectra for the CD1/PI film are presented in Figure S21. The absorption peak is centered at 380 nm, and a strong blue emission at 450 nm without shifting is observable between $\lambda_{ex}$ = 300 nm and $\lambda_{ex}$ = 420 nm. Figure 4 shows the ASE characteristics. The dependence of the output intensity on the pumping fluence indicates a clear ASE threshold around 400 kW/cm$^2$, above which the film exhibits an ASE peak around 458 nm and a narrow fwhm of about 16 nm. A blue ASE spot can be seen (inset in Figure 4b). The ASE threshold of the CD1/PI film is higher than that of the CD1 solution, which may be due to the fact that the concentration of the CD1/PI solution and the film thickness were not optimized. For the waveguide structure, the influence of the film thickness on the ASE threshold is obvious.[50,51] On the other hand, the minimum fwhm of the CD1/PI film is larger than that of the CD1 solution (4 nm); this difference is most likely due to the reflectances of the two end planes of the cuvette (∼5%), which constitutes a weak Fabry−Perot cavity and plays a key role in the longitudinal mode selection.[22,52] To the best of our knowledge, this is the first observation of CD-based ASE in a planar waveguide structure. We expect that it will be practical and convenient for CD-based lasing devices.

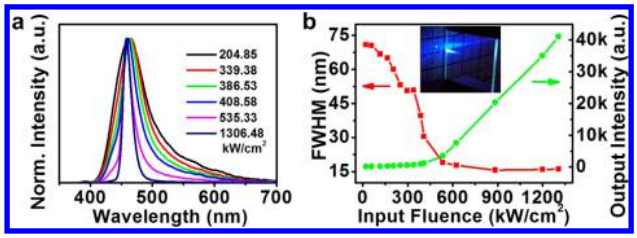


**Figure 4.** ASE characteristics of CD1/PI film. (a) Normalized emission spectra of CD1/PI film with different pumping fluences. (b) Dependence of the output peak intensity and fwhm of CD1/PI on the pumping fluence. The inset in (b) depicts the operating device pumped at 355 nm for the CD1/PI film.

## CONCLUSIONS

We proposed that the ASE thresholds of CDs are strongly correlated with their PL emission characteristics rather than with their FLQYs. Specifically, CDs with $\lambda_{ex}$-independent PL characteristics are more likely than CDs with $\lambda_{ex}$-dependent PL characteristics to realize ASE. This difference likely originates from the different amounts of C−O−H/C−O−C groups in the two types of CDs since these groups can introduce numerous related localized electronic states, which would decentralize the excited electrons, thus increasing the difficulty of population inversion. It is strongly recommended that excess C−O−H/C−O−C groups be avoided when synthesizing and selecting CDs for low-threshold ASE or lasing. The CDs with $\lambda_{ex}$-independent PL characteristics also exhibited $K_R$ values and SECs higher than those of CDs with $\lambda_{ex}$-dependent PL characteristics. Moreover, ASE in a planar waveguide structure formed from CDs with $\lambda_{ex}$-independent PL characteristics was successfully demonstrated and could be highly practical and convenient in CD-based solid-state laser devices.

## ASSOCIATED CONTENT

### Supporting Information

The Supporting Information is available free of charge on the ACS Publications website at DOI: 10.1021/acsami.6b08315.

Scheme of preparation; heating curve; XRD spectra; FT-IR spectra; XPS spectra; contour plot of PL spectra; schematic diagram of experimental setup for laser pumping investigations; ASE spectra; PL decay curves; absorption, PL spectra of the CDs (PDF)


DOI: 10.1021/acsami.6b08315
ACS Appl. Mater. Interfaces 2016, 8, 25454−25460

## AUTHOR INFORMATION


### Corresponding Authors

*E-mail: huyongsheng@ciomp.ac.cn (Y.H.).
*E-mail: fanyi@ciomp.ac.cn (Y.F.).
*E-mail: liuxy@ciomp.ac.cn (X.L.).


### Notes

The authors declare no competing financial interest.

## ACKNOWLEDGMENTS

This work was funded by the CAS Innovation Program, National Natural Science Foundation of China No. 6140031454, Jilin Province Science and Technology Research Project No. 20140520119JH and 20150101039JC, and project supported by State Key Laboratory of Luminescence and Applications.

## REFERENCES


(1) Baker, S. N.; Baker, G. A. Luminescent Carbon Nanodots: Emergent Nanolights. *Angew. Chem., Int. Ed.* **2010**, *49*, 6726−6744.

(2) Jiang, K.; Sun, S.; Zhang, L.; Lu, Y.; Wu, A.; Cai, C.; Lin, H. Blue Luminescence by Carbon Dots: Full-Color Emission Tuning and Multicolor Cellular Imaging. *Angew. Chem., Int. Ed.* **2015**, *54*, 5360−5363.

(3) Dong, Y.; Pang, H.; Yang, H. B.; Guo, C.; Shao, J.; Chi, Y.; Li, C. M.; Yu, T. Carbon-Based Dots Co-doped with Nitrogen and Sulfur for High Quantum Yield and Excitation-Independent Emission. *Angew. Chem., Int. Ed.* **2013**, *52*, 7800−7804.

(4) Wang, L.; Zhu, S.-J.; Wang, H.-Y.; Qu, S.-N.; Zhang, Y.-L.; Zhang, J.-H.; Chen, Q.-D.; Xu, H.-L.; Han, W.; Yang, B.; et al. Common Origin of Green Luminescence in Carbon Nanodots and Graphene Quantum Dots. *ACS Nano* **2014**, *8*, 2541−2547.

(5) Zhu, S.; Meng, Q.; Wang, L.; Zhang, J.; Song, Y.; Jin, H.; Zhang, K.; Sun, H.; Wang, H.; Yang, B. Highly Photoluminescent Carbon Dots for Multicolor Patterning, Sensors, and Bioimaging. *Angew. Chem., Int. Ed.* **2013**, *52*, 3953−3957.

(6) Qu, D.; Zheng, M.; Zhang, L.; Zhao, H.; Xie, Z.; Jing, X.; Haddad, R. E.; Fan, H.; Sun, Z. Formation Mechanism and Optimization of Highly Luminescent N-Doped Graphene Quantum Dots. *Sci. Rep.* **2014**, *4*, 5294.

(7) Zheng, M.; Xie, Z.; Qu, D.; Li, D.; Du, P.; Jing, X.; Sun, Z. On-Off-On Fluorescent Carbon Dot Nanosensor for Recognition of Chromium (VI) and Ascorbic Acid Based on the Inner Filter Effect. *ACS Appl. Mater. Interfaces* **2013**, *5*, 13242−13247.

(8) Cao, L.; Wang, X.; Meziani, M. J.; Lu, F.; Wang, H.; Luo, P. G.; Lin, Y.; Harruff, B. A.; Veca, L. M.; Murray, D.; et al. Carbon Dots for Multiphoton Bioimaging. *J. Am. Chem. Soc.* **2007**, *129*, 11318−11319.

(9) Sun, Y. P.; Zhou, B.; Lin, Y.; Wang, W.; Fernando, K. S.; Pathak, P.; Meziani, M. J.; Harruff, B. A.; Wang, X.; Wang, H.; et al. Quantum-Sized Carbon Dots for Bright and Colorful Photoluminescence. *J. Am. Chem. Soc.* **2006**, *128*, 7756−7757.

(10) Yang, S. T.; Wang, X.; Wang, H.; Lu, F.; Luo, P. G.; Cao, L.; Meziani, M. J.; Liu, J. H.; Liu, Y.; Chen, M.; et al. Carbon Dots as Nontoxic and High-Performance Fluorescence Imaging Agents. *J. Phys. Chem. C* **2009**, *113*, 18110−18114.

(11) Pan, L.; Sun, S.; Zhang, A.; Jiang, K.; Zhang, L.; Dong, C.; Huang, Q.; Wu, A.; Lin, H. Truly Fluorescent Excitation-Dependent Carbon Dots and Their Applications in Multicolor Cellular Imaging and Multidimensional Sensing. *Adv. Mater.* **2015**, *27*, 7782−7787.

(12) Qu, S.; Wang, X.; Lu, Q.; Liu, X.; Wang, L. A Biocompatible Fluorescent Ink Based on Water-Soluble Luminescent Carbon Nanodots. *Angew. Chem., Int. Ed.* **2012**, *51*, 12215−12218.

(13) Jiang, K.; Zhang, L.; Lu, J.; Xu, C.; Cai, C.; Lin, H. Triple-Mode Emission of Carbon Dots: Applications for Advanced Anti-Counterfeiting. *Angew. Chem.* **2016**, *128*, 7347.

(14) Wang, F.; Chen, Y.; Liu, C.; Ma, D. White Light-Emitting Devices Based on Carbon Dots' Electroluminescence. *Chem. Commun.* **2011**, *47*, 3502−3504.

(15) Zhang, X.; Zhang, Y.; Wang, Y.; Kalytchuk, S.; Kershaw, S. V.; Wang, Y.; Wang, P.; Zhang, T.; Zhao, Y.; Zhang, H.; et al. Color-Switchable Electroluminescence of Carbon Dot Light-Emitting Diodes. *ACS Nano* **2013**, *7*, 11234−11241.

(16) Liu, J.; Liu, Y.; Liu, N.; Han, Y.; Zhang, X.; Huang, H.; Lifshitz, Y.; Lee, S.-T.; Zhong, J.; Kang, Z. Metal-Free Efficient Photocatalyst for Stable Visible Water Splitting via a Two-Electron Pathway. *Science* **2015**, *347*, 970−974.

(17) Zhang, W. F.; Jin, L. M.; Yu, S. F.; Zhu, H.; Pan, S. S.; Zhao, Y. H.; Yang, H. Y. Wide-Bandwidth Lasing from C-dot/Epoxy Nanocomposite Fabry-Perot Cavities with Ultralow Threshold. *J. Mater. Chem. C* **2014**, *2*, 1525−1531.

(18) Nie, H.; Li, M.; Li, Q.; Liang, S.; Tan, Y.; Sheng, L.; Shi, W.; Zhang, S. X.-A. Carbon Dots with Continuously Tunable Full-Color Emission and Their Application in Ratiometric pH Sensing. *Chem. Mater.* **2014**, *26*, 3104−3112.

(19) Ding, H.; Yu, S.-B.; Wei, J.-S.; Xiong, H.-M. Full-Color Light-Emitting Carbon Dots with a Surface-State-Controlled Luminescence Mechanism. *ACS Nano* **2016**, *10*, 484−491.

(20) Zhang, W.; Zhu, H.; Yu, S.; Yang, H. Observation of Lasing Emission from Carbon Nanodots in Organic Solvents. *Adv. Mater.* **2012**, *24*, 2263−2267.

(21) Zhu, H.; Zhang, W.; Yu, S. F. Realization of Lasing Emission from Graphene Quantum Dots using Titanium Dioxide Nanoparticles as Light Scatterers. *Nanoscale* **2013**, *5*, 1797−1802.

(22) Qu, S.; Liu, X.; Guo, X.; Chu, M.; Zhang, L.; Shen, D. Amplified Spontaneous Green Emission and Lasing Emission from Carbon Nanoparticles. *Adv. Funct. Mater.* **2014**, *24*, 2689−2695.

(23) Schultz, T.; Quenneville, J.; Levine, B.; Toniolo, A.; Martínez, T. J.; Lochbrunner, S.; Schmitt, M.; Shaffer, J. P.; Zgierski, M. Z.; Stolow, A. Mechanism and Dynamics of Azobenzene Photoisomerization. *J. Am. Chem. Soc.* **2003**, *125*, 8098−8099.

(24) Hu, S.; Trinchi, A.; Atkin, P.; Cole, I. Tunable Photoluminescence Across the Entire Visible Spectrum from Carbon Dots Excited by White Light. *Angew. Chem., Int. Ed.* **2015**, *54*, 2970−2974.

(25) Zhang, M.; Bai, L.; Shang, W.; Xie, W.; Ma, H.; Fu, Y.; Fang, D.; Sun, H.; Fan, L.; Han, M.; Liu, C.; Yang, S. Facile Synthesis of Water-Soluble, Highly Fluorescent Graphene Quantum Dots as a Robust Biological Label for Stem Cells. *J. Mater. Chem.* **2012**, *22*, 7461−7467.

(26) Guo, Y.; Wang, Z.; Shao, H.; Jiang, X. Hydrothermal Synthesis of Highly Fluorescent Carbon Nanoparticles from Sodium Citrate and Their Use for the Detection of Mercury Ions. *Carbon* **2013**, *52*, 583−589.

(27) Dong, Y.; Shao, J.; Chen, C.; Li, H.; Wang, R.; Chi, Y.; Lin, X.; Chen, G. Blue Luminescent Graphene Quantum Dots and Graphene Oxide Prepared by Tuning the Carbonization Degree of Citric Acid. *Carbon* **2012**, *50*, 4738−4743.

(28) Wen, Z.-H; Yin, X.-B. Excitation-Independent Carbon Dots, from Photoluminescence Mechanism to Single-Color Application. *RSC Adv.* **2016**, *6*, 27829−27835.

(29) Tang, L.; Ji, R.; Cao, X.; Lin, J.; Jiang, H.; Li, X.; Teng, K.; Luk, C. M.; Zeng, S.; Hao, J.; et al. Deep Ultraviolet Photoluminescence of Water-Soluble Self-Passivated Graphene Quantum Dots. *ACS Nano* **2012**, *6*, 5102−5110.

(30) Liu, S.; Tian, J.; Wang, L.; Zhang, Y.; Qin, X.; Luo, Y.; Asiri, A. M.; Al-Youbi, A. O.; Sun, X. Hydrothermal Treatment of Grass: a Low-Cost, Green Route to Nitrogen-Doped, Carbon-Rich, Photoluminescent Polymer Nanodots as an Effective Fluorescent Sensing Platform for Label-Free Detection of Cu (II) Ions. *Adv. Mater.* **2012**, *24*, 2037−2041.

(31) Xu, F.; Minniti, M.; Barone, P.; Sindona, A.; Bonanno, A.; Oliva, A. Nitrogen Doping of Single Walled Carbon Nanotubes by Low Energy Ion Implantation. *Carbon* **2008**, *46*, 1489−1496.

(32) Sheng, Z. H.; Shao, L.; Chen, J.-J.; Bao, W. J.; Wang, F.-B.; Xia, X. H. Catalyst-Free Synthesis of Nitrogen-Doped Graphene via Thermal Annealing Graphite Oxide with Melamine and Its Excellent Electrocatalysis. *ACS Nano* **2011**, *5*, 4350−4358.

(33) Weng, L.; Poleunis, C.; Bertrand, P.; Carlier, V.; Sclavons, M.; Franquinet, P.; Legras, R. Sizing Removal and Functionalization of the




DOI: 10.1021/acsami.6b08315
*ACS Appl. Mater. Interfaces* 2016, 8, 25454−25460

Carbon Fiber Surface Studied by Combined TOF SIMS and XPS. *J. Adhes. Sci. Technol.* **1995**, *9*, 859−871.
(34) Gardner, S. D.; Singamsetty, C. S.; Booth, G. L.; He, G.-R.; Pittman, C. U. Surface Characterization of Carbon Fibers using Angle-Resolved XPS and ISS. *Carbon* **1995**, *33*, 587−595.
(35) Sun, J.; Yang, S.; Wang, Z.; Shen, H.; Xu, T.; Sun, L.; Li, H.; Chen, W.; Jiang, X.; Ding, G.; Kang, Z.; Xie, X.; Jiang, M. Ultra-High Quantum Yield of Graphene Quantum Dots: Aromatic-Nitrogen Doping and Photoluminescence Mechanism. *Part. Part. Syst. Charact.* **2015**, *32*, 434−440.
(36) Sun, H.; Wu, L.; Gao, N.; Ren, J.; Qu, X. Improvement of Photoluminescence of Graphene Quantum Dots with a Biocompatible Photochemical Reduction Pathway and Its Bioimaging Application. *ACS Appl. Mater. Interfaces* **2013**, *5*, 1174−1179.
(37) Cushing, S. K.; Li, M.; Huang, F.; Wu, N. Origin of Strong Excitation Wavelength Dependent Fluorescence of Graphene Oxide. *ACS Nano* **2014**, *8*, 1002−1013.
(38) Zhu, S.; Zhang, J.; Tang, S.; Qiao, C.; Wang, L.; Wang, H.; Liu, X.; Li, B.; Li, Y.; Yu, W.; et al. Surface Chemistry Routes to Modulate the Photoluminescence of Graphene Quantum Dots: From Fluorescence Mechanism to Up-Conversion Bioimaging Applications. *Adv. Funct. Mater.* **2012**, *22*, 4732−4740.
(39) Gan, Z.; Xiong, S.; Wu, X.; Xu, T.; Zhu, X.; Gan, X.; Guo, J.; Shen, J.; Sun, L.; Chu, P. K. Mechanism of Photoluminescence from Chemically Derived Graphene Oxide: Role of Chemical Reduction. *Adv. Opt. Mater.* **2013**, *1*, 926−932.
(40) Yan, J.-A.; Xian, L.; Chou, M. Y. Structural and Electronic Properties of Oxidized Graphene. *Phys. Rev. Lett.* **2009**, *103*, 086802.
(41) Chien, C.-T.; Li, S.-S.; Lai, W.-J.; Yeh, Y.-C.; Chen, H.-A.; Chen, I. S.; Chen, L.-C.; Chen, K.-H.; Nemoto, T.; Isoda, S.; Chen, M.; Fujita, T.; Eda, G.; Yamaguchi, H.; Chhowalla, M.; Chen, C.-W. Tunable Photoluminescence from Graphene Oxide. *Angew. Chem., Int. Ed.* **2012**, *51*, 6662−6666.
(42) Shaklee, K. L.; Leheny, R. F. Direct Determination of Optical Gain in Semiconductor Crystals. *Appl. Phys. Lett.* **1971**, *18*, 475−477.
(43) Nakanotani, H.; Furukawa, T.; Adachi, C. Light Amplification in an Organic Solid-State Film with the Aid of Triplet-to-Singlet Upconversion. *Adv. Opt. Mater.* **2015**, *3*, 1381−1388.
(44) Liu, F.; Jang, M.-H.; Ha, H. D.; Kim, J.-H.; Cho, Y.-H.; Seo, T. S. Facile Synthetic Method for Pristine Graphene Quantum Dots and Graphene Oxide Quantum Dots: Origin of Blue and Green Luminescence. *Adv. Mater.* **2013**, *25*, 3657−3662.
(45) Yang, B.; Mao, X.; Yang, S.; Li, Y.; Wang, Y.; Wang, M.; Deng, W.; Han, K. Low Threshold Two-Photon-Pumped Amplified Spontaneous Emission in $CH_3NH_3PbBr_3$ Microdisks. *ACS Appl. Mater. Interfaces* **2016**, *8*, 19587−19592.
(46) Adachi, C.; Nakanotani, H. Organic Semiconductor Laser Materials. *Mater. Matters* **2009**, *4*, 74.
(47) Aimono, T.; Kawamura, Y.; Goushi, K.; Yamamoto, H.; Sasabe, H.; Adachi, C. 100% Fluorescence Efficiency of 4, 4′-Bis [(N-Carbazole) Styryl] Biphenyl in a Solid Film and the Very Low Amplified Spontaneous Emission Threshold. *Appl. Phys. Lett.* **2005**, *86*, 071110.
(48) Forget, S.; Chénais, S. *Organic Solid-State Lasers*; Springer: London, 2013.
(49) She, C.; Fedin, I.; Dolzhnikov, D. S.; Demortière, A.; Schaller, R. D.; Pelton, M.; Talapin, D. V. Low-Threshold Stimulated Emission Using Colloidal Quantum Wells. *Nano Lett.* **2014**, *14*, 2772−2777.
(50) Costela, A.; García, O.; Cerdán, L.; García-Moreno, I.; Sastre, R. Amplified Spontaneous Emission and Optical Gain Measurements From Pyrromethene 567-Doped Polymer Waveguides and Quasi-Waveguides. *Opt. Express* **2008**, *16*, 7023−7036.
(51) Calzado, E. M.; Villalvilla, J. M.; Boj, P. J.; Quintana, J. A.; Díaz-García, M. A. Tuneability of Amplified Spontaneous Emission Through Control of the Thickness in Organic-Based Waveguides. *J. Appl. Phys.* **2005**, *97*, 093103.
(52) Howell, B. F.; Kuzyk, M. G. Lasing Action and Photodegradation of Disperse Orange 11 Dye in Liquid Solution. *Appl. Phys. Lett.* **2004**, *85*, 1901.


DOI: 10.1021/acsami.6b08315
*ACS Appl. Mater. Interfaces* 2016, 8, 25454−25460